ACS APPLIED MATERIALS & INTERFACES

Forum Article

www.acsami.org

$FeSb_2$–Al_2O_3–C Nanocomposite Anodes for Lithium-Ion Batteries

Eric Allcorn and Arumugam Manthiram*

Materials Science and Engineering Program & Texas Materials Institute The University of Texas at Austin Austin, Texas 78712, United States

ABSTRACT: $FeSb_2$–Al_2O_3–C nanocomposite synthesized by ambient-temperature high-energy mechanical milling (HEMM) of Sb_2O_3, Fe, Al, and C has been investigated as an anode material for lithium-ion batteries. The $FeSb_2$–Al_2O_3–C nanocomposites are characterized with X-ray diffraction (XRD), X-ray photoelectron spectroscopy (XPS), scanning electron microscopy (SEM), and high-resolution transmission electron microscopy (HRTEM). The characterization data reveal it to be composed of crystalline $FeSb_2$ nanoparticles finely dispersed in an amorphous matrix of Al_2O_3 and carbon. The $FeSb_2$–Al_2O_3–C nanocomposite exhibits an initial discharge (lithiation) capacity of 877 mAh g^{-1} and an initial charge (delithiation) capacity of 547 mAh g^{-1}, yielding an initial coulombic efficiency of 62%. The extended cycling performance for this composite is far superior to that of the intermetallic $FeSb_2$ or a similarly prepared $FeSb_2$–C composite. $FeSb_2$–Al_2O_3–C retains a specific capacity of ~350 mAh g^{-1} after 500 lithiation/delithiation cycles.

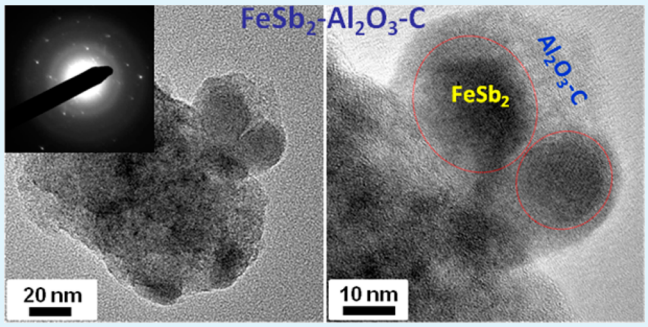

KEYWORDS: *lithium-ion battery, alloy anode, intermetallic, iron antimonide, mechanochemical reaction*

INTRODUCTION

Lithium-ion batteries have been instrumental to the development of portable electronics and much of the current research focuses on improving their capabilities so that they can expand to other applications such as transportation or stationary storage. The conventional anode material in most commercial lithium-ion batteries today is graphitic carbon. However, the limited capacity (372 mAh g^{-1}), low tap density (< 1 g cm^{-3}), and safety issues related to the low reaction potential vs. Li/Li^+ of graphite necessitate the search for new anode materials for future lithium-ion batteries.

Lithium alloying materials have undergone intensive study as potential anodes for lithium-ion batteries. Because each atom in these alloy anodes is capable of reacting with one or more Li atoms, they possess extremely high theoretical capacities (e.g., $Li_{4.4}Si$, 4200 mAh g^{-1}; $Li_{4.4}Sn$, 990 mAh g^{-1}; and Li_3Sb, 660 mAh g^{-1}). In addition, some of these materials, particularly Sb, generally react with lithium at higher potentials vs. Li/Li^+, which could help suppress solid-electrolyte interphase (SEI) layer formation and eliminate lithium plating risks, thereby mitigating safety hazards. Safety is a critical issue for the adoption of lithium-ion technology for large-scale applications: transportation and stationary storage. However, the primary factor inhibiting the adoption of alloy anodes is the extremely large volume change they undergo upon lithiation/delithiation.[1,2] The large volume change results in mechanical strain and crumbling of the active electrode particles, leading to loss of electrical contact throughout the material and rapid capacity fade, usually within a small number of cycles. Approaches pursued to negate these effects include the use of intermetallic alloys instead of pure alloying material, reduction of active material dimensions, and the incorporation of a mechanically reinforcing matrix.[1−12]

Intermetallics intended for lithium anode application—such as NiSb, $FeSn_2$, Cu_2Sb, and $FeSb_2$—are typically composed of an active component and an electrochemically inactive component bonded together. The reaction of these materials with lithium proceeds via one of two reaction types: a conversion reaction or an addition reaction. In a conversion reaction, such as with NiSb or $FeSn_2$, the inactive component is extruded to form a conductive and reinforcing matrix while the reaction of lithium with the active component proceeds as usual, shown respectively in reactions 1 and 2[3−5]

$$M_xSb \rightarrow xM + Sb \quad (1)$$

$$xM + Sb + 3Li \rightarrow xM + Li_3Sb \quad (2)$$

In an addition reaction, such as with Cu_2Sb or $FeSb_2$, lithium is incorporated into the original material to form a ternary phase and one of the initial components may be partially extruded to achieve a favorable stoichiometry.[6−11] For example, Cu_2Sb reacts to form Li_2CuSb with one atom of Cu extruded. The generalized reaction is shown in reaction 3

$$M_xSb + yLi \rightarrow zM + Li_yM_{(x-z)}Sb \quad (3)$$

Special Issue: New Materials and Approaches for Electrochemical Storage

Received: January 21, 2014
Accepted: March 17, 2014
Published: March 24, 2014

Frequently, as is the case with both Cu_2Sb and $FeSb_2$, the initial addition reaction is followed by a conversion reaction that extrudes the remaining inert metal to form the final lithiation product of the active element. Both forms of intermetallics have demonstrated improved cyclability over pure active elements, but certain addition reactions with structural relations between the reaction phases have proven especially effective.[7] In addition, the lithiation reaction is not always fully reversible, with the final delithiation product frequently being a mixture of the pure active and inactive elements instead of the original intermetallic alloy.[10,11]

The reduction of active material dimensions—through particle size reduction or the creation of a nanoscale architecture—has shown to improve the performance of alloy anodes.[1,2] Because of the large surface area to volume ratio at such small scales, the volume expansion/contraction of the material can be accommodated without causing a build-up of internal stresses that lead to mechanical failure. This is especially true for mismatch stresses incurred during phase change, as occurs in lithium alloying materials.[13] However, particle agglomeration is an issue over extended cycling and can lead to a loss of the benefits instilled by the small-dimension active materials.

Electrochemically inert metals and ceramics can be incorporated into a composite with an active material to provide mechanical support during the lithiation/delithiation reaction and to absorb some of the induced stresses, preventing crumbling of the active material.[2,5,8,12] Electrochemically active materials are also applied for this purpose. A secondary advantage of these reinforcing matrices is that if they are well incorporated with nanoscale active materials they can act as a barrier to prevent the agglomeration of active particles during cycling, extending the benefits of using a nano-scale active material.[5,8,12] Accordingly, in this study, we combine the benefits of these three approaches into a single composite system of $FeSb_2$–Al_2O_3–C with a single-step synthesis process to achieve a long cycle life in an alloy anode material with improved volumetric and specific capacity relative to graphite.

EXPERIMENTAL SECTION

$FeSb_2$–Al_2O_3–C nanocomposite was synthesized by mixing a stoichiometric ratio of the precursor powders Fe (Alfa Aesar, 99.9%, <10 μm), Sb_2O_3 (Alfa Aesar, 99.6%, 1.1–1.8 μm), and Al (Alfa Aesar, 99%, 17–30 μm), along with 20 wt % acetylene black carbon (Alfa Aesar, 99.99%, −200 mesh). Because of a negative free energy change, the milling process mechanochemically induces reaction 4

$$Fe + Sb_2O_3 + 2Al \rightarrow FeSb_2 + Al_2O_3 \quad \Delta G^\circ = -1010\ \text{kJ mol}^{-1} \tag{4}$$

The precursor mixture underwent 48 h of high-energy mechanical milling (HEMM) under an argon atmosphere at room temperature with a ball:powder ratio of 20:1 and a milling speed of 500 rpm. For the incorporation of heat treatment into the synthesis of $FeSb_2$–Al_2O_3–C, the same stoichiometric mixture of Fe, Sb_2O_3, and Al underwent 24 h of HEMM under the same conditions outlined previously but without the presence of 20 wt % acetylene black carbon. After this initial HEMM step, the material was subjected to 8 h of heat treatment at 400 °C in an aluminum oxide crucible under flowing argon. Then 20 wt % acetylene black carbon was mixed with this material and the combined powder underwent a second HEMM step of 24 h under the same previously mentioned conditions.

The resulting electrode powder was characterized by XRD analysis to determine the phases present with a Philips X-ray Diffractometer and Cu–Kα radiation. X-ray photoelectron spectroscopy (XPS) was used to confirm the presence of desired amorphous phases with a Kratos XPS and a monochromatic Al–Kα source. Powder morphology was analysed by scanning electron microscopy (SEM) with a JEOL JSM-5610 equipment and high-resolution transmission electron microscopy (HRTEM) with a JEOL 2010F equipment. In addition, ex situ XRD was carried out on electrodes under different states of charge. These electrode samples were prepared by opening the cycled coin cells inside an Ar-filled glovebox and placing them under a protective polyimide film for analysis on a Rigaku X-ray Diffractometer with Cu–Kα radiation.

To measure the electrochemical performances of $FeSb_2$–Al_2O_3–C and related materials, test electrodes were cast onto a copper foil substrate with the doctor blade method with slurries consisting of 70 wt % active powder, 15 wt % polyvinylidene fluoride (PVDF) dissolved in N-methyl pyrrolidone (NMP) as a binder, and 15 wt % conductive carbon (Super P). The electrodes were dried for 12 h at 120 °C in a vacuum oven. CR2032 coin cells were then assembled in an Ar-filled glovebox with the cast electrode as the working electrode, Celgard polypropylene as the separator, lithium foil as the counter/reference electrode, and 1 M $LiPF_6$ in ethylene carbonate (EC)/diethyl carbonate (DEC) (1 : 1 v/v) as the electrolyte. Discharge/charge cycling of these cells was carried out with an Arbin battery cycler with a constant current density of 100 mA g^{-1} (roughly C/4) over a voltage window of 0–2 V vs. the lithium reference.

RESULTS AND DISCUSSION

XRD characterization of the as-synthesized $FeSb_2$–Al_2O_3–C powder, shown in Figure 1, shows it to contain crystalline

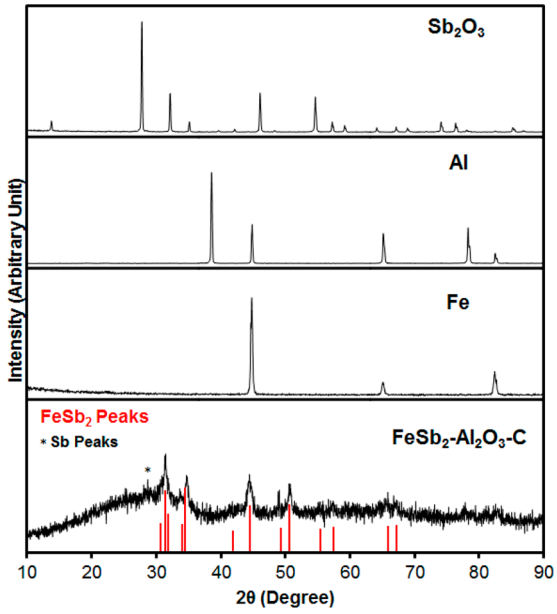

Figure 1. XRD patterns of the precursor powders and the as-synthesized composite powder $FeSb_2$–Al_2O_3–C, showing the only crystalline peaks present to be those of the active intermetallic $FeSb_2$ with a very small residual peak of metallic Sb.

particles of active $FeSb_2$ intermetallic phase. The $FeSb_2$ thus formed is the orthorhombic seinajokite phase (space group: Pnnm) with unit cell dimensions of a = 5.82 Å, b = 6.5194 Å, and c = 3.188 Å (JCPDS File: 34-1184). Aside from small residual Sb peaks, no other precursor materials remain and no other crystalline phases are observed. However, in Figure 2 XPS analysis of the electrode powder shows a shift in the Al 2p binding energy from the value of 72.8 eV for metallic Al to the observed peak of 74.7 eV that correlates to and confirms the presence of amorphous Al_2O_3.[14] This analysis confirms that our composite contains both an active intermetallic and a

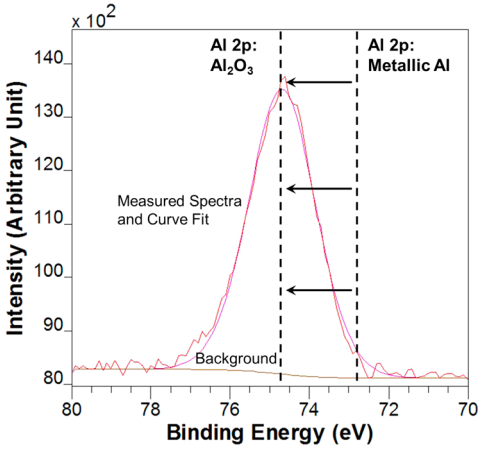

Figure 2. XPS analysis of as-synthesized $FeSb_2$–Al_2O_3–C showing the binding energy shift in the Al-2p peak to 74.7 eV, matching the expected binding energy value for Al_2O_3.[14]

mechanically reinforcing matrix, as intended. Figure 3 shows the HRTEM images of the as-synthesized $FeSb_2$–Al_2O_3–C,

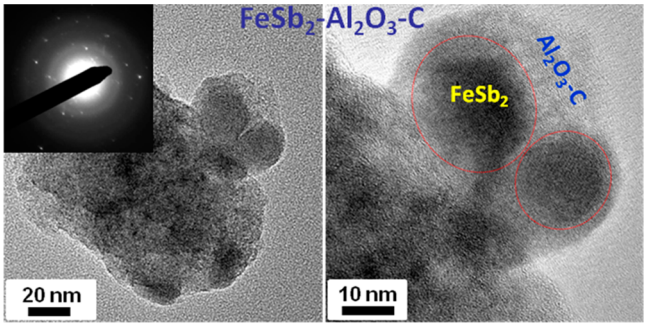

Figure 3. HRTEM images of as-synthesized $FeSb_2$–Al_2O_3–C nanocomposite anode, showing crystalline particles of $FeSb_2$ with sizes of ~10 nm dispersed within an amorphous matrix of Al_2O_3 and carbon.

indicating the presence of active $FeSb_2$ particles of roughly 20 nm diameter surrounded by the amorphous matrix of Al_2O_3 and carbon. This confirms the presence of nano-scale active material and demonstrates the effective intermixing of the secondary matrix with active particles due to the mechano-chemically induced in situ formation of Al_2O_3. This intermixing allows the Al_2O_3 and carbon matrix to provide especially effective mechanical reinforcement, accommodating the volume change of the active particles while also serving to separate them and inhibit their agglomeration during extended cycling.

On the basis of the ratio of the precursors used for the synthesis of $FeSb_2$–Al_2O_3–C, the as-synthesized nanocomposite material is composed of 60 wt % $FeSb_2$, 20 wt % Al_2O_3, and 20 wt % carbon. It also has a relatively high practical tap density of 1.3 g cm^{-3} compared to the graphite anode (< 1 g cm^{-3}), yielding enhanced volumetric capacity.

In the first cycle, the $FeSb_2$–Al_2O_3–C nanocomposite anode material exhibits initial discharge and charge capacities of, respectively, 877 mAh g^{-1} and 547 mAh g^{-1}, resulting in an initial coulombic efficiency of 62%. Figure 4a shows the voltage vs capacity plot of $FeSb_2$–Al_2O_3–C during the first five discharge/charge cycles and Figure 4b shows the same information for the HEMM-synthesized pure $FeSb_2$. $FeSb_2$ intermetallic was recently shown to react with lithium via an addition reaction producing the phase $Li_4Fe_{0.5}Sb_2$ + 0.5Fe followed by a conversion reaction producing the final products of Fe + $2Li_3Sb$.[9,10] For fully discharged $FeSb_2$–Al_2O_3–C, ex situ XRD analysis shows no discernible crystalline peaks due to very fine crystalline particles and/or the small amount of sample in the electrode. However, in Figure 5, ex situ XRD

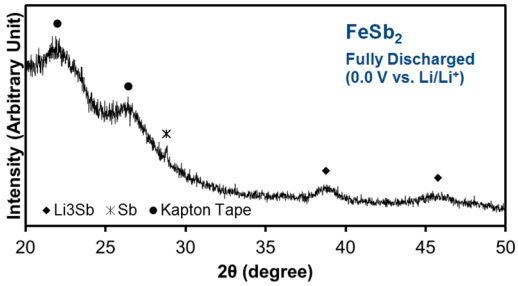

Figure 5. Ex situ XRD pattern of a pure $FeSb_2$ intermetallic electrode that has been fully discharged (lithiated) to 0.0 V vs. Li/Li^+ showing the lithiation product phase Li_3Sb.

analysis of the fully discharged $FeSb_2$ intermetallic shows peaks corresponding to Li_3Sb, confirming the final reaction products. The similarity between the $FeSb_2$–Al_2O_3–C and pure $FeSb_2$ reaction curves after the initial cycle suggests that the same reaction products should be present in the nanocomposite as well, but are not detectable by XRD due to very small particle size or poor crystallinity. Although the first cycle for $FeSb_2$–Al_2O_3–C exhibits a large irreversible capacity loss, the

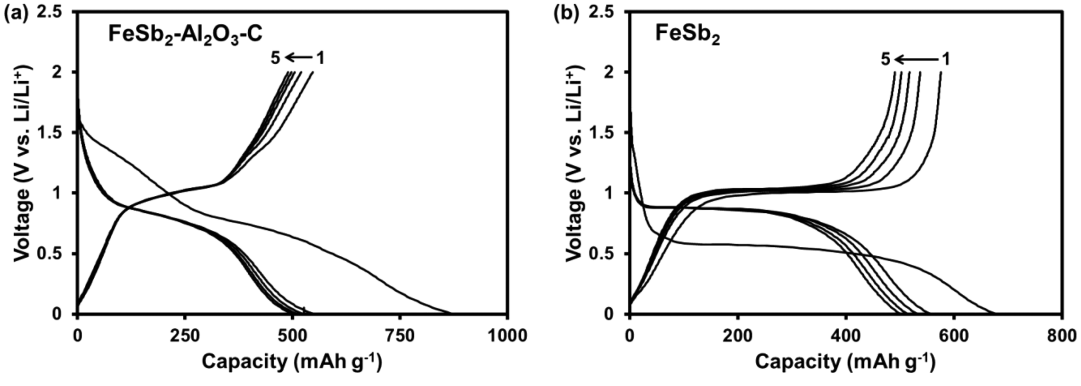

Figure 4. Voltage vs. capacity plots of (a) $FeSb_2$–Al_2O_3–C and (b) $FeSb_2$ intermetallic electrodes over the first several cycles.

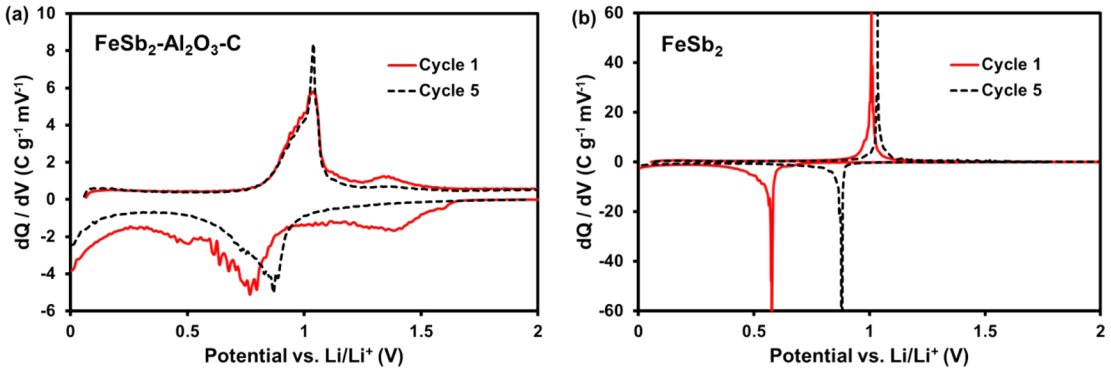

Figure 6. Differential capacity plots (DCPs) of (a) $FeSb_2$−Al_2O_3−C and (b) $FeSb_2$ intermetallic electrodes over their 1st and 5th cycles.

subsequent cycles show good reversibility with little capacity loss. Some sources of this large irreversible capacity loss are incomplete reduction of Sb_2O_3 during synthesis resulting in Li_2O formation, SEI layer formation at low potentials, and side reactions with amorphous Al_2O_3 + carbon matrix.[15,16] Pure $FeSb_2$ has a smaller irreversibility than $FeSb_2$−Al_2O_3−C, but it exhibits worse capacity retention after the initial cycle due to the lack of an inert reinforcing phase to control the volume change effects. After the initial cycle, the primary reaction plateaus of both materials match very closely with those of metallic Sb. This suggests that after the initial alloying reaction to form Li_3Sb and Fe, there is no subsequent reformation of the $FeSb_2$ intermetallic phase upon delithiation. The products of the first cycle delithiation are metallic Sb and metallic Fe, and later cycles are simply the alloying/dealloying reaction of metallic Sb. This is in agreement with previously published results for $FeSb_2$.[11]

Figures 6a and b show, respectively, the differential capacity plots (DCP) for $FeSb_2$−Al_2O_3−C and $FeSb_2$. The irreversible reaction peak for the formation of Li_2O is observable in the initial discharge curve of $FeSb_2$−Al_2O_3−C at ∼1.4 V vs. Li/Li^+.[15,17] As would be expected, this peak is not observed in the pure $FeSb_2$ DCP curve. The initial discharge curve for pure $FeSb_2$ has a primary peak that closely matches previously published data. However, our data show no secondary lithiation peak at 0.4 V that is present in some studies. This peak has been shown to be rate dependent and only present in materials with large crystallite size, so it appears our samples are cycled at a fast enough rate and/or have a small enough particle size that the peak does not present itself.[9,11] The initial discharge peaks for $FeSb_2$−Al_2O_3−C are noticeably shifted from those observed in the pure intermetallic. Some of the shift can be attributed to the nano-scale active material and composite system, and the higher onset potential for lithiation is most likely due to the residual metallic Sb in the system as evidenced in the XRD pattern shown in Figure 1. However, more in-depth analysis of this reaction may be warranted to determine if the reaction mechanism of the $FeSb_2$ system is altered when incorporated into this nanocomposite. There is also a noticeable increase in storage capacity for $FeSb_2$−Al_2O_3−C as it approaches a potential of 0.0 V vs. Li/Li^+. This is related to the reversible lithiation of the carbon material incorporated into the nanocomposite. As discussed previously, the peaks for the 5th cycle closely match those observed for metallic antimony for both materials.

Although the large irreversible capacity suffered in the first cycle of the $FeSb_2$−Al_2O_3−C material is a significant issue, there are options to address and control those losses. A previously published nickel antimonide composite anode demonstrated significantly reduced first cycle losses when a heat treatement step was incorporated into the synthesis process.[5] This heat treatment step facilitates a more complete reduction of the residual Sb_2O_3, thereby limiting the losses at high potential due to the formation of Li_2O. As shown in Table 1, first cycle improvements are also observed in our $FeSb_2$−Al_2O_3−C anode when a heat treatment step is incorporated as described in the Experimental Section. The heat treatment is applied as an intermediate step such that the final material morphology is minimally affected, as demonstrated in Figure 7 with the SEM images of $FeSb_2$−Al_2O_3−C powders with and without heat treatment. In both cases, the powder is composed of roughly spherical agglomerates (smaller than 2 μm) of particles. The voltage vs. capacity plot is shown in Figure 8 for the heat-treated $FeSb_2$−Al_2O_3−C. The heat treatment has minimal effect as the curve shape and the primary plateau potentials are essentially the same as in Figure 4a. The primary difference is the smaller irreversible capacity loss at higher potentials during first cycle, which is a result of the reduction of residual Sb_2O_3 during the heat treatment step. In addition, there is no demonstrated negative impact on the cycle life of the nanocomposite anode.

Table 1. Initial Cycle Performances of $FeSb_2$−Al_2O_3−C with and without a Heat Treatment Step during Synthesis, Demonstrating the Ability of Heat Treatment to Reduce First Cycle Irreversible Loss

	irreversible capacity (mAh g^{-1})	reversible capacity (mAh g^{-1})	first cycle losses (mAh g^{-1})	initial Coulombic efficiency (%)
$FeSb_2$−Al_2O_3−C with no heat treatment	877	547	330	62
$FeSb_2$−Al_2O_3−C with 400 °C heat treatment	812	575	237	71

It should also be noted that the reaction peak for $FeSb_2$ lies at a relatively high potential, with roughly 75% of the capacity lying above 0.5 V vs. Li/Li^+ after the initial cycle (70% for $FeSb_2$−Al_2O_3−C). This gives $FeSb_2$ active materials the potential to operate over a raised voltage window, which could mitigate some effects of SEI layer formation and essentially eliminate the risk of lithium plating. Some negative effects of higher voltage cycling are reduced capacity and energy storage capabilities, as well as the likely need for a conditioning cycle that would result in higher first cycle irreversibilities.[9]

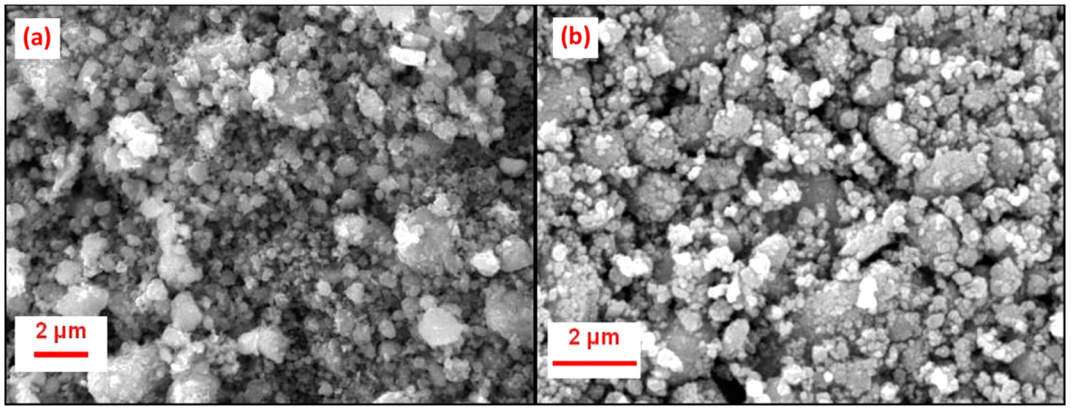

Figure 7. SEM images of the $FeSb_2$–Al_2O_3–C (a) after heat treatment at 400°C and (b) without heat treatment.

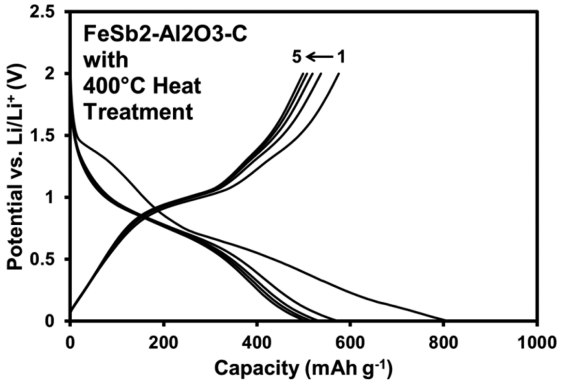

Figure 8. Voltage vs. capacity plots of the first several cycles of $FeSb_2$–Al_2O_3–C that has undergone 8 h of heat treatment at 400 °C under flowing argon.

Electrochemical impedance spectroscopy (EIS) analysis was carried out on $FeSb_2$–Al_2O_3–C, $FeSb_2$–C, and heat-treated $FeSb_2$–Al_2O_3–C. Figure 9a and b show, respectively, the Nyquist plots for these samples after an initial conditioning cycle and after 10 cycles. For all three samples, the impedance curves are composed of two semicircles at high frequency and a linear region at lower frequencies. The two semi-circles correspond to the surface layer diffusion and charge-transfer resistance of the electrodes, while the linear region corresponds to the bulk lithium diffusion through the electrode. After one cycle, Figure 9a shows that the impedance of the heat-treated $FeSb_2$–Al_2O_3–C is the lowest in all regions, the $FeSb_2$–Al_2O_3–C sample without heat treatment is slightly higher in all regions, and $FeSb_2$–C is the highest. After 10 cycles, Figure 9b shows that the impedance of all three samples has increased, although the increase is significantly larger for $FeSb_2$–C than for $FeSb_2$–Al_2O_3–C or heat treated $FeSb_2$–Al_2O_3–C. This impedance growth is most likely due to SEI layer formation and growth on the electrode surfaces. For both the Al_2O_3 containing electrodes, the growth is smaller possibly due to volume change mitigation effects that inhibit new surface exposure during cycling, coating of active particles by Al_2O_3, and a lower surface reactivity due to the inclusion of the inert Al_2O_3.

Cycle life data shown in Figure 10a compares the long-term performance of $FeSb_2$–Al_2O_3–C to a similarly prepared $FeSb_2$–C composite as well as to pure $FeSb_2$ intermetallic electrodes. This performance metric highlights most effectively the value of the reinforcing Al_2O_3 matrix in improving the performance of the $FeSb_2$ intermetallic. While the pure intermetallic and intermetallic/carbon composite suffer total cell failure prior to 100 cycles, $FeSb_2$–Al_2O_3–C maintains useful capacity for several hundred cycles, demonstrating a capacity of roughly 350 mAh g^{-1} even after 500 cycles. This drastic performance improvement shows the capability of the $FeSb_2$–Al_2O_3–C nanocomposite system to control volume change losses in the lithium alloying material as well as the

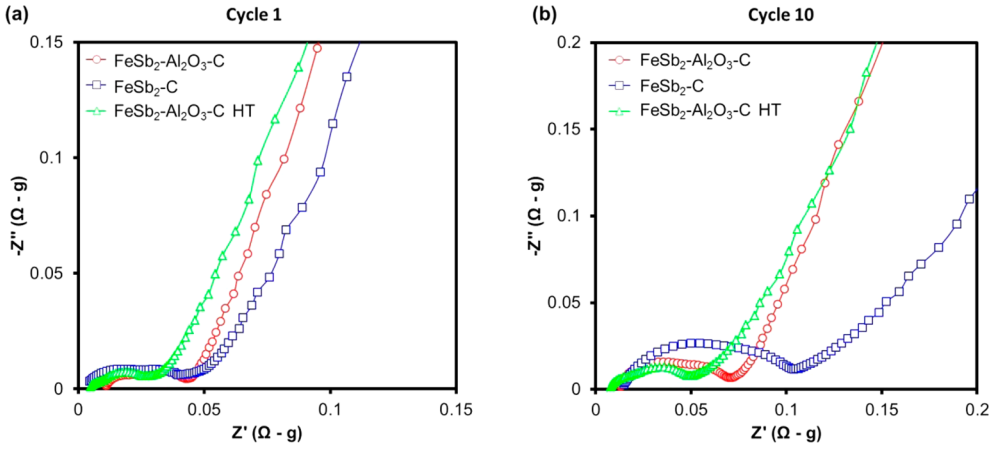

Figure 9. Nyquist plots of $FeSb_2$–Al_2O_3–C, $FeSb_2$–C, and heat treated (400 °C) $FeSb_2$–Al_2O_3–C (denoted as $FeSb_2$–Al_2O_3–C HT) (a) after an initial conditioning cycle and (b) after 10 charge/discharge cycles.

dx.doi.org/10.1021/am500448f | ACS Appl. Mater. Interfaces 2014, 6, 10886–10891

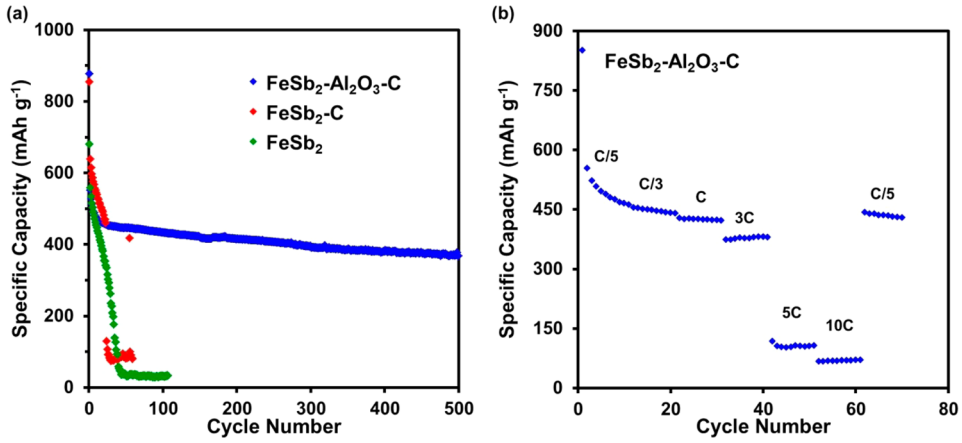

Figure 10. (a) Comparison of the cycle life performances of $FeSb_2$−Al_2O_3−C, $FeSb_2$−C, and $FeSb_2$, demonstrating the extended cycle life provided by the Al_2O_3 + C matrix. (b) Rate capability performances of $FeSb_2$−Al_2O_3−C at various *C*-rates.

effectiveness of the Al_2O_3 + C matrix in inhibiting extensive particle agglomeration during cycling. Figure 10b shows the rate capability of this material to be good up to 3C, with a capacity retention of 87 % at 1.2 A g^{-1} (3*C*). However, at higher rates of 5*C* and 10*C*, the electronically insulating nature of the Al_2O_3 matrix leads to a drastic reduction in performance.

CONCLUSIONS

Overall, this work has demonstrated that the $FeSb_2$−Al_2O_3−C nanocomposite synthesized by HEMM offers dramatic improvement in the cycle life of typical alloy anode materials through the employment of multiple volume change mitigation techniques: intermetallic active material, nano-scale active particles, and a mechanically reinforcing buffer matrix. While the first cycle losses are quite high in this material, techniques such as heat treatment during synthesis are capable of addressing this to a degree. Overall, the extended cycle life, good rate capability, and high tap density of $FeSb_2$−Al_2O_3−C give it much promise as a Li-ion battery anode, whereas its high operating potential make it capable of operating effectively under safer cycling conditions.

AUTHOR INFORMATION

Corresponding Author

*E-mail: rmanth@mail.utexas.edu. Phone: (512) 471-1791. Fax: (512) 471-7681.

Notes

The authors declare no competing financial interest.

ACKNOWLEDGMENTS

This work was supported by the U.S. Department of Energy, Office of Basic Energy Sciences, Division of Materials Sciences and Engineering, under Award DE-SC0005397.

REFERENCES

(1) Ji, L.; Lin, Z.; Alcoutlabi, M.; Zhang, X. Recent Developments in Nanostructured Anode Materials for Rechargeable Lithium-Ion Batteries. *Energy Environ. Sci* **2011**, *4*, 2682−2699.

(2) Zhang, W.-J. A Review of the Electrochemical Performance of Alloy Anodes for Lithium-Ion Batteries. *J. Power Sources* **2011**, *196*, 13−24.

(3) Chamas, M.; Sougrati, M.-T.; Reibel, C.; Lippens, P.-E. Quantitative Analysis of the Initial Restructuring Step of Nanostructured $FeSb_2$-Based Anodes for Li-Ion Batteries. *Chem. Mater.* **2013**, *25*, 2410−2420.

(4) Ionica, C. M.; Lippens, P. E.; Fourcade, J. O.; Jumas, J.-C. Study of Li Insertion Mechanisms in Transition Metal Antimony Compounds as Negative Electrodes for Li-Ion Battery. *J. Power Sources* **2005**, *146*, 478−481.

(5) Allcorn, E.; Manthiram, A. NiSb-Al_2O_3-C Nanocomposite Anodes with Long Cycle Life for Li-Ion Batteries. *J. Phys. Chem. C* **2014**, *118*, 811−822.

(6) Morcrette, M.; Larcher, D.; Tarascon, J. M.; Edstrom, K.; Vaughey, J. T.; Thackeray, M. M. Influence of Electrode Microstructure on the Reactivity of Cu_2Sb with Lithium. *Electrochim. Acta* **2007**, *52*, 5339−5345.

(7) Fransson, L. M. L.; Vaughey, J. T.; Benedek, R.; Edstrom, K.; Thomas, J. O.; Thackeray, M. M. Phase Transitions in Lithiated Cu_2Sb Anodes for Lithium Batteries: An In Situ X-Ray Diffraction Study. *Electrochem. Commun.* **2001**, *3*, 317−323.

(8) Applestone, D.; Yoon, S.; Manthiram, A. Cu_2Sb-Al_2O_3-C Nanocomposite Alloy Anodes with Exceptional Cycle Life for Lithium Ion Batteries. *J. Mater. Chem.* **2012**, *22*, 3242−3248.

(9) Villevieille, C.; Fraisse, B.; Womes, M.; Jumas, J.-C.; Monconduit, L. A New Ternary Li_4FeSb_2 Structure Formed upon Discharge of the $FeSb_2$/Li Cell. *J. Power Sources* **2009**, *189*, 324−330.

(10) Villevieille, C.; Ionica-Bousquet, C. M.; Fraisse, B.; Zitoun, D.; Womes, M.; Jumas, J. C.; Monconduit, L. Comparative Study of $NiSb_2$ and $FeSb_2$ as Negative Electrodes for Li-Ion Batteries. *Solid State Ionics* **2011**, *192*, 351−355.

(11) Park, C.-M.; Sohn, H.-J. Antimonides ($FeSb_2$, $CrSb_2$) with Orthorhombic Structure and Their Nanocomposites for Rechargeable Li-Ion Batteries. *Electrochim. Acta* **2010**, *55*, 4987−4994.

(12) Yoon, S.; Manthiram, A. Sb-MO_x-C (M = Al, Ti, or Mo) Nanocomposite Anodes for Lithium-Ion Batteries. *Chem. Mater.* **2009**, *21*, 3898−3904.

(13) Huggins, R. A.; Nix, W. D. Decrepitation Model for Capacity Loss during Cycling of Alloys in Rechargeable Electrochemical Systems. *Ionics* **2000**, *6*, 57−63.

(14) Moulder, J.; Stickle, W.; Sobol, P.; Bomben, K. *Handbook of X-Ray Photoelectron Spectroscopy*; Physical Electronics Inc.: Eden Prairie, MN, 1995.

(15) Li, H.; Huang, X.; Chen, L. Anodes Based on Oxide Materials for Lithium Rechargeable Batteries. *Solid State Ionics* **1999**, *123*, 189−197.

(16) Jung, S. C.; Han, Y.-K. How Do Li Atoms Pass through the Al_2O_3 Coating Layer during Lithiation in Li-Ion Batteries? *J. Phys. Chem. Lett.* **2013**, *4*, 2681−2685.

(17) Xue, M.-Z.; Fu, Z.-W. Electrochemical Reaction of Lithium with Nanostructured Thin Film of Antimony Trioxide. *Electrochem. Commun.* **2006**, *8*, 1250−1256.